Normal Modes of Redox-Active Tyrosine: Conformation Dependence and Comparison to Experiment

Kevin Range,[†] Idelisa Ayala,[‡] Darrin York,[§] and Bridgette A. Barry*,[||]

Department of Chemistry, Lock Haven University of Pennsylvania, Lock Haven, Pennsylvania 17745, Department of Natural Sciences, Broward Community College, Davie, Florida, 33314, Department of Chemistry, University of Minnesota, 207 Pleasant St. SE, Minneapolis, Minnesota 55455-0431, School of Chemistry and Biochemistry and the Petit Institute for Bioengineering and Bioscience, Georgia Institute of Technology, Atlanta, Georgia 30332

Received: March 10, 2006; In Final Form: April 6, 2006

Redox-active tyrosine residues play important roles in long-distance electron reactions in enzymes such as prostaglandin H synthase, ribonucleotide reductase, and photosystem II (PSII). Spectroscopic characterization of tyrosyl radicals in these systems provides a powerful experimental probe into the role of the enzyme in mediation of long-range electron transfer processes. Interpretation of such data, however, relies critically on first establishing a spectroscopic fingerprint of isotopically labeled tyrosinate and tyrosyl radicals in nonenzymatic environments. In this report, FT-IR results obtained from tyrosinate, tyrosyl radical (produced by ultraviolet photolysis of polycrystalline tyrosinate), and their isotopologues at 77 K are presented. Assignment of peaks and isotope shifts is aided by density-functional B3LYP/6-311++G(3df,2p)//B3LYP/6-31++G-(d,p) calculations of tyrosine and tyrosyl radical in several different charge and protonation states. In addition, characterization of the potential energy surfaces of tyrosinate and tyrosyl radical as a function of the backbone and ring torsion angles provides detailed insight into the sensitivity of the vibrational frequencies to conformational changes. These results provide a detailed spectroscopic interpretation, which will elucidate the structures of redox-active tyrosine residues in complex protein environments. Specific application of these data is made to enzymatic systems.

1. Introduction

Redox-active tyrosine residues play an important role in many electron-transfer enzymes such as prostaglandin H synthase,[1] ribonucleotide reductase,[2] and photosystem II (PSII).[3,4] Oxidation of tyrosine or tyrosinate results in a neutral tyrosyl radical, which can act as an intermediate in electron transfer. The environmental factors responsible for functional control of these redox-active species have not as yet been elucidated.[5]

A variety of optical and magnetic resonance spectroscopies can be used to study the structure of tyrosyl and phenoxyl radicals by ultraviolet photolysis in model compounds (see ref 5 for a review). Electron paramagnetic resonance (EPR) studies of the tyrosyl radical indicate that the majority of the spin density is located on carbons 1′, 3′, and 5′ and on the phenolic oxygen.[6−10] Raman vibrational studies have demonstrated that formation of the radical is associated with a decrease in frequency for a ring stretching vibration and with an increase in the C−O stretching frequency.[11−14]

Quantum chemical calculations have also proven to be useful tools to study tyrosyl radicals.[15−23] Most theoretical studies to date have considered phenoxyl radical or other "truncated tyrosine" models (e.g., *p*-methylphenoxyl radical) for the full tyrosyl radical. There have been relatively few studies that have considered explicitly the effect of the amino acid backbone, including intramolecular backbone−side chain interactions and conformational dependence.[16,22] While most of the spin density of tyrosyl resides on the aromatic ring, the small amount of spin density on the peptide backbone does have a noticeable effect on the vibrations of the radical.[4,16,22,24]

In this report, a detailed analysis of the vibrations of tyrosinate, tyrosyl radical, and several of their isotopologues using density-functional theory is presented, along with their experimentally determined FT-IR spectra. The following combination of experimental and calculated data represents the most comprehensive exploration of the vibrations of these systems to date. Both the radical and ground-state species are characterized with a consistent, high-quality level of theory; key degrees of conformational freedom are exhaustively explored; and eight isotopologues are analyzed. These results are compared to vibrational spectra associated with the oxidation of a redox active tyrosine in PSII, the photosynthetic water splitting enzyme.

2. Materials and Methods

2.1. Calculations. Electronic structure calculations were performed on tyrosine and tyrosyl radical in several different charge and protonation states in the gas phase with Kohn−Sham density-functional theory (DFT) using the hybrid exchange functional of Becke[25,26] and the Lee, Yang, and Parr correlation functional[27] (B3LYP) and the 6-31++G(d,p) basis set.[28] All electronic structure calculations were performed with the *Gaussian 98* suite of programs.[29] Integrals involving the exchange-correlation potential used the default numerical integration mesh with a maximum of 75 radial shells and 302

* bridgette.barry@chemistry.gatech.edu.
[†] Lock Haven University of Pennsylvania.
[‡] Broward Community College.
[§] University of Minnesota.
[||] Georgia Institute of Technology.

10.1021/jp061503f CCC: $33.50
Published on Web 05/17/2006

angular quadrature points per shell pruned to approximately 7000 points per atom.[30] Geometry optimizations were done in redundant internal coordinates with the default convergence criteria.[31] Frequencies were calculated from the analytic Hessians using the facilities in *Gaussian 98* and are not scaled. Tighter geometry convergence criteria and finer integration meshes had very little effect on the calculated frequencies.

Hybrid density functionals such as B3LYP have been shown to give excellent results for radical systems similar to the tyrosyl radicals considered here[15,17−21,32,33] and are so reliable for more mundane species that they are used to calculate the geometry and frequencies for many multilevel methods such as CBS-QB3,[34] G3B3,[35] and W1.[36] B3LYP/6-31++G(d,p) geometries and frequencies are also used in the QCRNA model chemistry, which has been used in various studies of phosphates and related biological systems.[37−40]

In an effort to benchmark the applied level of theory (B3LYP/6-31++G(d,p)), the vibrational spectrum of phenoxyl radical, a well-studied compound related to the present system,[41,42] was computed. The geometry of phenoxyl radical at several different levels of theory is shown in Table S-1 of the Supporting Information. As might be predicted from previous calculations on this molecule, the B3LYP/6-31++G(d,p) geometry predicts a slightly elongated carbon−oxygen bond. In other respects, however, the B3LYP/6-31++G(d,p) geometry agrees very well with the previous reports.[41,42] Experimental and calculated vibrational frequencies of the phenoxyl radical are shown in Table S-2 of the Supporting Information. The B3LYP/6-31++G(d,p) vibrational frequencies match the previously reported B3LYP/cc-pVTZ numbers quite well. From this, we conclude that B3LYP/6-31++G(d,p) is an adequate level of theory to predict vibrational frequencies and isotope shifts for molecules of this type.

The effects of isotopic substitution on the vibrational spectra were calculated using vibrational projection analysis (ViPA).[43] Eigenvectors and eigenvalues were read from the *Gaussian 98* output in the high-precision format (10^{-5} Å) for each of the isotopologues. The mass-weighted eigenvectors of the isotopically substituted structures, $\underline{Q}$, were then projected onto the mass-weighted eigenvectors of the unsubstituted structure, $\underline{B}$, giving a matrix of projection coefficients, $\underline{\underline{C}}$, whose elements, $c_{j,k}$ are given by

$$c_{j,k} = \underline{Q}_j^T \cdot \underline{B}_k \tag{1}$$

The percent similarity between a substituted mode and an unsubstituted mode is given by

$$c_{j,k}^{\%} = 100 c_{j,k}^2 \tag{2}$$

since all of the eigenvectors in question are normalized.

In addition to the B3LYP/6-31++G(d,p) vibrational analysis, B3LYP/6-311++G(3df,2p) single-point calculations were performed to provide refined energies and natural bond order analysis.[44,45]

2.2. Experimental. L-Tyrosine was from Sigma (St. Louis, MO). L-Tyrosine-4′-ring-^{13}C (99.3%), L-tyrosine-ring-$^{13}C_6$ (98−99%), L-tyrosine-ring-D_4 (98%), L-tyrosine-^{15}N (98.9%), and L-tyrosine-$^{13}C_1(\alpha)$ (99.2%) were from Cambridge Isotope Laboratories (Andover, MA). L-4-Hydroxyphenyl-3,5-D_2-alanine (98.2%) was from MSD Isotopes (Montreal, Canada). L-[4′-^{18}O]-Tyrosine (93.7%) and L-[4′-^{17}O]-tyrosine (^{17}O, 33.7%; ^{18}O, 29%) were from the National Stable Isotopes Resource at Los Alamos National Laboratory (Los Alamos, NM). Mass spectrometry measurements were performed on a Bruker Daltonics Biflex III MALDI-TOF spectrometer (Billerica, MA). The isotopic composition for L-tyrosine-phenol-4-^{13}C, L-tyrosine-^{15}N, L-4-hydroxyphenyl-3,5-D_2-alanine, L-[4′-^{18}O]-tyrosine, and L-[4′-^{17}O]-tyrosine were verified by this method. Boric acid was purchased from EM Science (Cherry Hill, NJ), and sodium borate was purchased from Mallinckrodt (Phillipsburg, NJ). Solutions of tyrosinate and isotopically labeled tyrosinate (100 mM) were prepared in 10 mM borate−NaOH, pH 11.

Reaction-induced FT-IR spectra were recorded on a Nicolet 60-SXR spectrometer equipped with a MCT-B detector (Nicolet, Madison, WI) and with a Hansen liquid nitrogen cryostat (R. G. Hansen & Associates, Santa Barbara, CA). Spectral conditions were as follows: resolution, 4 cm^{-1}; mirror velocity, 1.57 cm/s; apodization function, Happ−Genzel; levels of zero filling, one; data acquisition time, 1 min; and temperature, 77 K. Illumination was provided by an Nd:YAG laser at 266 nm (Continuum, Santa Clara, CA). Five laser flashes were employed with a frequency of 10 Hz and pulse energy of 35−37 mJ. The sample was partially dehydrated on a CaF_2 window. The UV spectrum (Hitachi, Danbury, CT) of the FT-IR sample was obtained, and the absorption band at 294 nm was used for normalization. Alternatively, the infrared bands at 1500 cm^{-1} or at 1260 cm^{-1} were used for normalization. The results obtained using all three methods were similar. Difference spectra, associated with the production of the radical, were constructed by subtracting data acquired before illumination from data acquired after illumination. Data were obtained on 2−8 different samples and were averaged. Difference spectra were found to be independent of concentration down to 10 mM.[46]

3. Results and Discussion

At pH 11, it is expected that tyrosine exists as a dianion, with both the carboxylic acid and phenol oxygens deprotonated. It is problematic to perform meaningful computations on tyrosine in this state in the gas phase due to the existence of positive eigenvalues for some of the occupied orbitals. (Occupied orbitals with positive eigenvalues are also found in Hartree−Fock (HF) and second-order Møller−Plesset (MP2) calculations of the tyrosinate dianion.) In light of this fact, several alternative model structures were investigated, including the use of continuum dielectric treatments of solvation and the inclusion of sodium ions or hydrogen-bonded waters at the phenol oxygen. All of these alternative structures predicted significant double-bond character for the phenol oxygen bond and failed to reliably model the experimental spectrum. Specifically, all of the alternative structures failed to model the intense $\upsilon_{7a'}$ peak at 1266 cm^{-1}, a distinctive and well-characterized feature of the tyrosinate vibrational spectrum.[5,12,13,22,23,47]

The structure shown in Figure 1a is stable in the gas phase (no positive occupied orbital eigenvalues) and reproduces all of the major feature of the experimental spectrum quite well. This phenol oxygen protonated structure should be viewed as a gas-phase *model* of the experimental conditions.

Upon photolysis at pH 11, it is expected that the resulting tyrosyl radical exists as an anion (Figure 1b). This state has no occupied orbitals with positive eigenvalues in the gas phase and therefore can serve as a model system in the present calculations. It might be argued that the phenol oxygen should be protonated for consistency with the chosen singlet structure; however, geometry optimizations in the gas phase of the "phenol oxygen

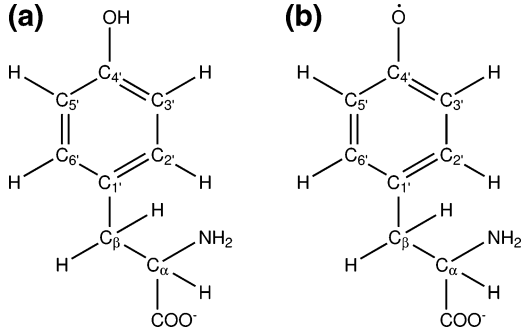

Figure 1. Model structures: (a) tyrosinate; (b) tyrosyl radical.

protonated" radical species resulted in decomposition at the carbonyl-α-carbon bond.

There is evidence, both experimental[48] and computational,[49] that the reduction and oxidation of tyrosine is tightly coupled to proton transfer. Previous experimental data suggest that the solvation shell is perturbed upon tyrosinate oxidation.[22]

3.1. Conformational Analysis. In an effort to explore the influence of conformation on the spectra, vibrational frequencies were computed for several conformations of the singlet (Figure 1a) and radical (Figure 1b) states. These conformations were determined by performing constrained geometry optimizations with the B3LYP/6-31G(d) model chemistry at 10° increments over the backbone ($C-C_\alpha-C_\beta-C_{1'}$) and ring ($C_\alpha-C_\beta-C_{1'}-C_{2'}$) dihedrals from −180° to 180° (0° to 170° for the radical ring dihedral due to symmetry). These potential energy surfaces (PES) are shown in Figure 2.

With these surfaces in hand, several unconstrained geometry optimization were run near each minimum with the B3LYP/6-31G(d) model chemistry. Unique B3LYP/6-31G(d) minima were then reoptimized with the target B3LYP/6-31++G(d,p) model chemistry and vibrational analysis performed for each unique minima. Single-point B3LYP/6-311++G(3df,2p) calculations were also done for each minimum to obtain refined energies for each conformer (Table 1).

The predicted conformations for the radical in Table 1 differ from that of Qin and Wheeler's SVWN/6-31G(d) and ROHF calculations in the ordering of conformers $\mathscr{A}$ and $\mathscr{B}$.[16] There are several reasons for this difference. Qin and Wheeler's calculations were performed on a neutral tyrosyl radical protonated at the carboxylate rather than the anion treated here. It is not surprising that the negatively charged carboxylate group in the present calcualtions will tend to prefer the conformation anti to the phenol ring more so than its neutral counterpart. Furthermore, the reliability of the level of theory in the present work is much better than those used previously. B3LYP is 1.3−4 times more accurate for bond lengths and 6−7 times more accurate for atomization energies than SVWN with similar basis sets.[50]

As seen in Table 1, B3LYP/6-311++G(3df,2p)//B3LYP/6-31++G(d,p) calculations predict that there are two stable conformers of tyrosine, with $C_\alpha-C_\beta-C_1'-C_2'$ dihedral angles of −102° and −110°. Experimental determination of the $C_\alpha-C_\beta-C_1'-C_2'$ dihedral angle distribution indicates that >90% of tyrosine exists in two conformations, one at −101° and one at −115°, which is 0.1 kcal/mol higher in energy,[51] in excellent agreement with conformers A and B in Table 1.

Warncke et al. have proposed that EPR line shape sensitivity to thermal annealing can be explained by conformational relaxation of the radical.[52] In these experiments, the $C_\alpha-C_\beta-C_1'-C_2'$ dihedral angle of the radical was observed to narrow when the sample was annealed. Examination of Table 1 and Figure 2 reveals an explanation of this phenomena from our calculations. In the ground state at room temperature, both conformations A and B (and their primed counterparts) are significantly populated. This conformational distribution is frozen when the sample is cooled in the experiment. Upon photolysis, A and A′ conformation tyrosines become $\mathscr{A}$ conformation tyrosyl radicals, while B and B′ conformation tyrosines find themselves in the $\mathscr{B}$ tyrosyl radical conformation, which is 2.6 kcal/mol higher in enthalpy. The $\mathscr{B}$ conformation radicals are trapped at cryogenic temperatures, but if annealed will fall into the $\mathscr{A}$ conformation, producing the EPR line shape shifts observed experimentally. Our work provides the first theoretical basis for these observations.

3.2. IR Spectra. Figure 3 presents the experimentally determined absorption spectra of tyrosinate (A), and the following isotopologues: $^{13}C_1(4')$ (B), $^{13}C_6$ (ring) (C), $^{2}H_4$ (ring) (D), 3′,5′-$^{2}H_2$ (ring) (E), $^{18}O_1$ (phenol) (F), $^{17}O_1$ (phenol) (G), $^{15}N_1$ (H), and $^{13}C_1(\alpha)$ (I) (See Methods for details). Comparison of these data identifies the magnitude of the isotope shifts in each isotopologue. Similarly, Figure 4 presents the photolysis-induced difference spectrum, tyrosyl radical minus tyrosinate, for natural abundance (B), and the following isotopologues: $^{13}C_1(4')$ (C), $^{13}C_6$ (ring) (D), $^{2}H_4$ (ring) (E), 3′,5′-$^{2}H_2$ (ring) (F), $^{18}O_1$ (phenol) (G), $^{17}O_1$ (phenol) (H), $^{15}N_1$ (I), and $^{13}C_1(\alpha)$ (J). As expected, the borate buffer alone (A) gave no defined vibrational features upon photolysis.

To more definitively identify isotope-shifted vibrational bands, the isotope-edited spectra were constructed for each isotopologue (Figure 5). To construct these data, the photolysis-induced difference spectra were subtracted, control minus isotopologue. Because the data were corrected for any small difference in path length and concentration, the difference spectra can be directly subtracted on a one-to-one basis. The only contributors to the isotope-edited spectra in Figure 5 are vibrational bands that are sensitive to photolysis and also to isotope labeling. This procedure can help to simplify complex difference spectra.

3.2.1. IR Spectra of Tyrosinate Isotopologues. Frequencies and isotope shifts for the tyrosinate ground state can be determined from Figure 3. In addtion, negative intensity bands in the isotope-edited spectra (Figure 5) arise from the tyrosinate ground state. Each negative intensity band is accompanied by an isotope-shifted positive intensity band. Examination of the isotope-edited spectra shows that the ground-state vibrational modes at 1602, 1500, 1266, and 1173 cm^{-1} and their isotope-shifted components are evident. Note that vibrational frequencies can be slightly shifted in the isotope-edited spectra, compared to the ground-state spectra (Figure 3), because differences in line shape and amplitude influence the subtracted frequencies. Isotope shifts in negative intensity bands in the 1350−1290 cm^{-1} region are also observed. These bands also arise from the ground-state tyrosinate molecule, but their assignment is not discussed here.

Table 2 shows the experimental and calculated vibrational frequencies for six modes for which the experimental isotope shifts were distinct (that is, not obscured by other peaks upon isotopic substitution), based on the spectra shown in Figures 3 and 5. These modes account for six of the seven most intense peaks in the experimental spectra. Also included for comparison are data from Nujol mull[53] and powder[54] infrared spectra of tyrosine.

It is interesting to note the influence of conformation on these modes. Three of the modes (ν_{8a}/NH_2 bend, ν_{19a}, and $\nu_{7a'}$ at 1602,

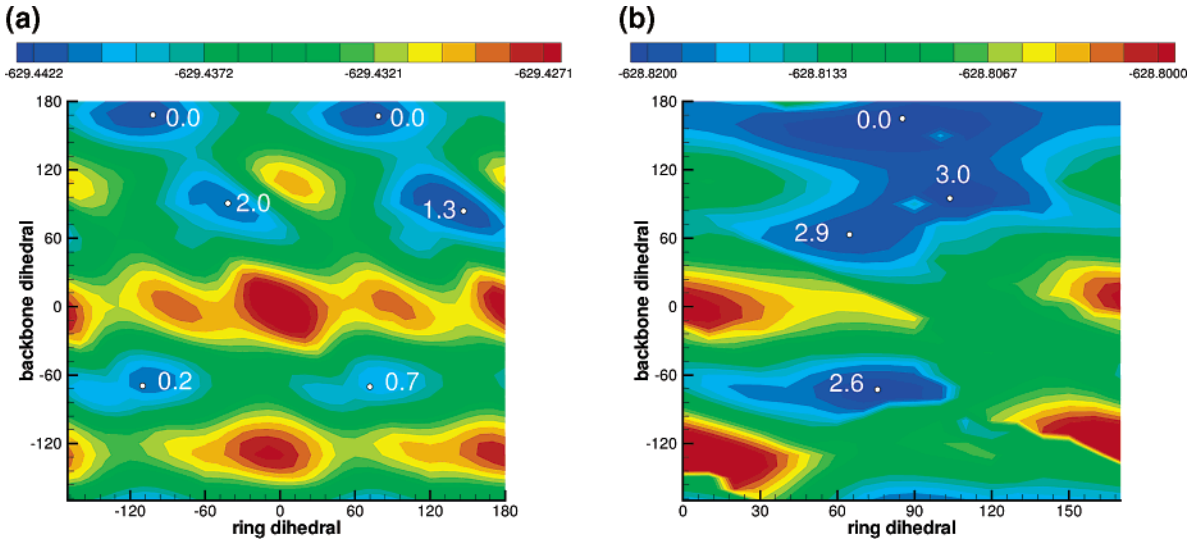

Figure 2. B3LYP/6-31G(d) potential energy surfaces (PES): (a) tyrosinate PES; (b) tyrosyl radical PES. White circles denote B3LYP/6-31++G-(d,p) optimized structures and are labeled with their relative B3LYP/6-311++G(3df,2p)//B3LYP/6-31++G(d,p) enthalpies (at 298.15 K) in kcal/mol. The contours are in hartrees.

TABLE 1: Conformer Relative Energies[a]

	ring[†]	bb[‡]	Newman[§]	E[¶]	E_0[‖]	H**
singlet						
A	-102	168	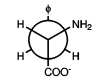	0.1	0.0	0.0
A′	77	167		0.1	0.0	0.0
B	-110	-69	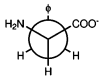	0.0	0.3	0.2
B′	72	-70		0.6	0.9	0.7
C	147	84	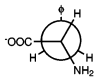	1.3	1.4	1.3
C′	-42	91		2.0	2.1	2.0
radical						
$\mathcal{A}$	85	165	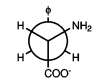	0.0	0.0	0.0
$\mathcal{B}$	76	-73	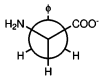	2.5	2.7	2.6
$\mathcal{C}$	65	63	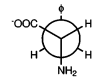	2.8	2.9	2.9
$\mathcal{D}$	103	95	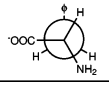	2.9	3.0	3.0

[a] All energies are in kcal/mol. For simple reference in the following tables and text, each conformer is given a symbol. Tyrosinate conformers which only differ in the ring dihedral by ~180° are distinguished with a slanted prime. [†] $C_\alpha-C_\beta-C_1'-C_2'$ dihedral angle in degrees. [‡] $C-C_\alpha-C_\beta-C_1'$ dihedral in degrees. [§] Newman projections of conformers looking down the $C_\alpha-C_\beta$ bond. [¶] B3LYP/6-311++G(3df,2p)//B3LYP/6-31++G(d,p). [‖] Zero-point corrected energy ($E + E_{ZPV}$). ** Enthalpy at 298.15 K.

1500, and 1266 cm^{-1}, respectively, in the experimental natural abundance spectrum) show some dependence on conformation (<10 cm^{-1} shifts). The other three modes (two NH_2 bend/COO^- asymmetric stretches and υ_{9a} at 1656, 1560, and 1173 cm^{-1} in the experimental natural abundance spectrum) shift by up to 34 cm^{-1} between the different conformations. The identification of conformation sensitive modes, which arise from the aromatic ring and C(4′)−O bond, will be able to help elucidate tyrosine conformations in polypeptides.[22,55−57]

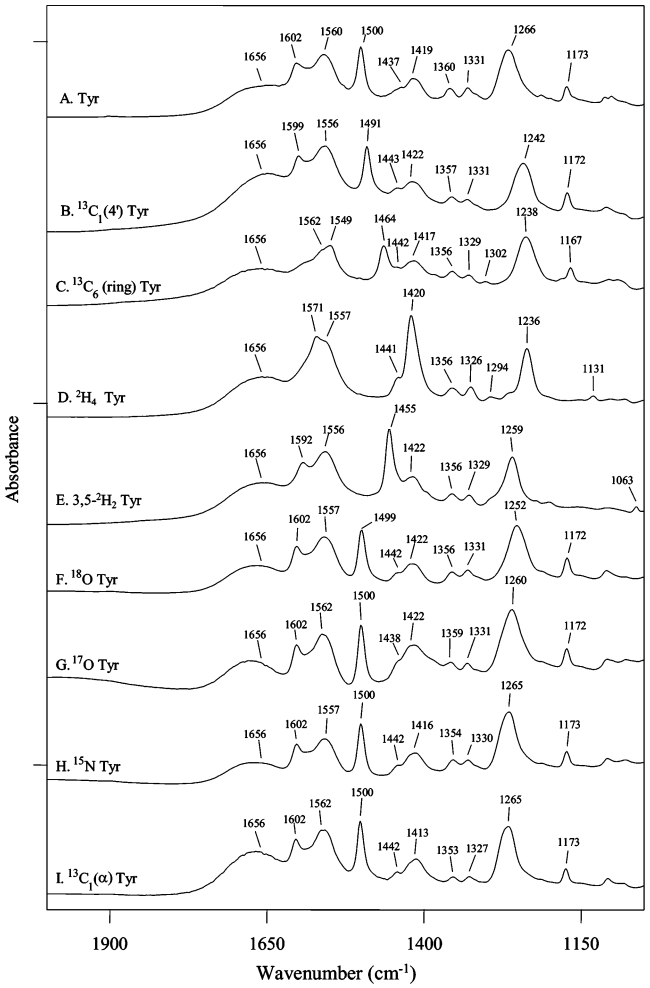

Figure 3. Infrared absorbance spectra of (A) tyrosinate, (B) $^{13}C_1$ (4′) tyrosinate, (C) $^{13}C_6$ (ring) tyrosinate, (D) $^{2}H_4$ (ring) tyrosinate, (E) 3′,5′-$^{2}H_2$ (ring) tyrosinate, (F) $^{18}O_1$ (phenol) tyrosinate, (G) $^{17}O_1$ (phenol) tyrosinate, (H) $^{15}N_1$ tyrosinate, and (I) $^{13}C_1(\alpha)$ tyrosinate. Borate buffer contributions were subtracted. See Experimental Section for spectral conditions. Tick marks on the *y*-axis represent 2 absorbance units.

Tables 3−6 show the experimental and calculated isotope shifts for the eight isotopologues studied. Calculated isotope shifts are presented for all modes which have greater than 10%

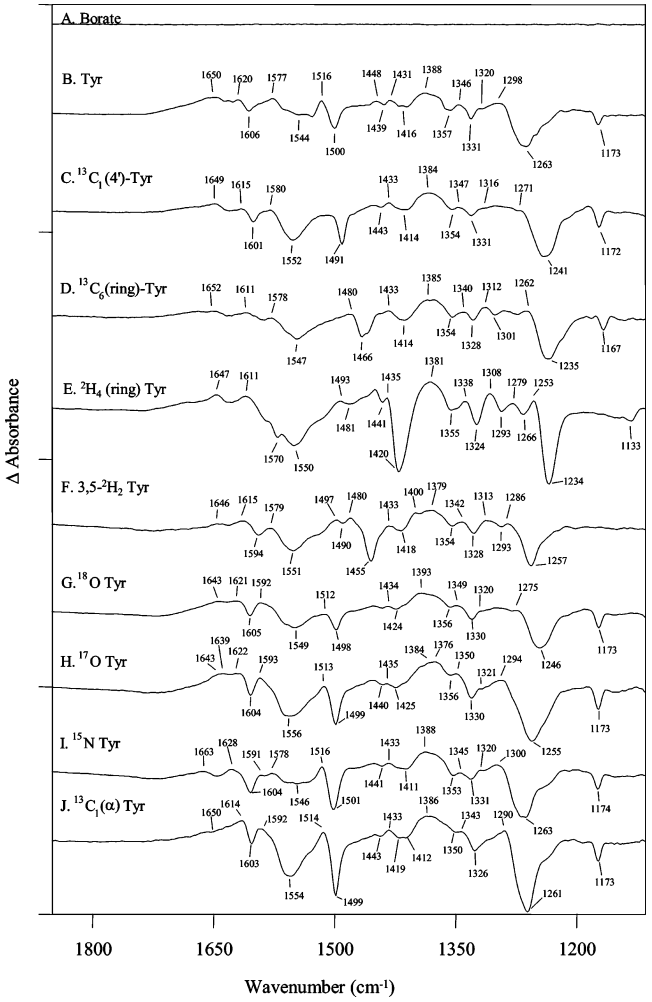

Figure 4. Difference FT-IR spectra associated with the UV photolysis of (A) borate buffer, (B) tyrosinate, (C) $^{13}C_1$ (4′-phenol) tyrosinate, (D) $^{13}C_6$ (ring) tyrosinate, (E) $^{2}H_4$ (ring) tyrosinate, (F) 3′,5′-$^{2}H_2$ (ring) tyrosinate, (G) $^{18}O_1$ (phenol) tyrosinate, (H) $^{17}O_1$ (phenol) tyrosinate, (I) $^{15}N_1$ tyrosinate, and (J) $^{13}C_1$ (α) tyrosinate. See Experimental Section for spectral conditions. Tick marks on the *y*-axis represent 0.05 absorbance units.

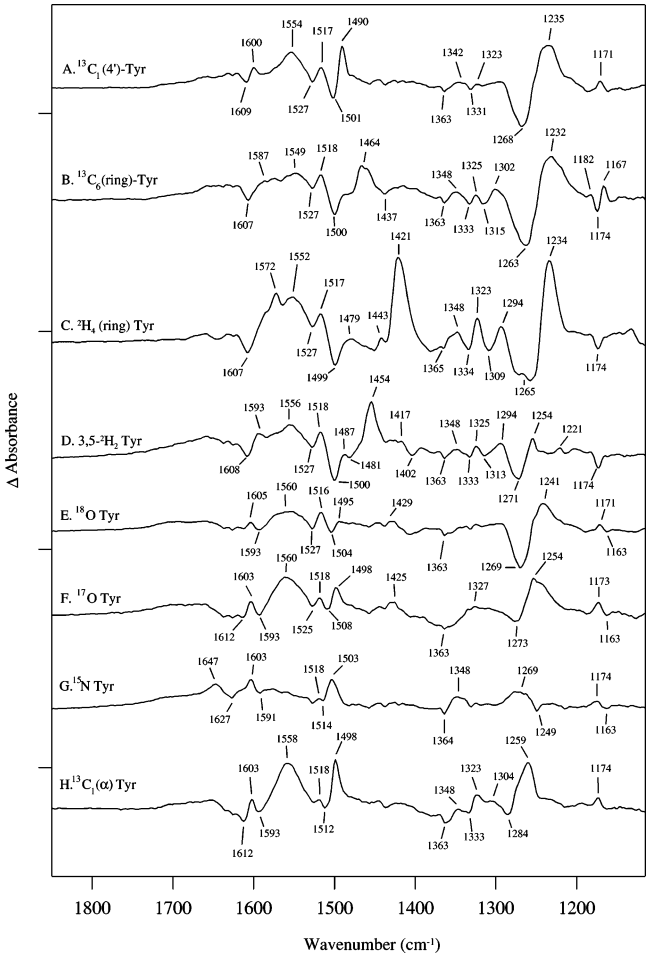

Figure 5. Isotope edited FT-IR spectra, reflecting the isotope sensitive bands in the photolysis spectrum of tyrosinate. The isotope edited spectra were constructed by one-to-one subtraction of the photolysis derived data, tyrosinate minus isotopologue. In each case, the isotopologue subtracted was (A) $^{13}C_1$ (4′-phenol) tyrosinate, (B) $^{13}C_6$ (ring) tyrosinate, (C) $^{2}H_4$ (ring) tyrosinate, (D) 3′,5′-$^{2}H_2$ (ring) tyrosinate, (E) $^{18}O_1$ (phenol) tyrosinate, (F) $^{17}O_1$ (phenol) tyrosinate, (G) $^{15}N_1$ tyrosinate, and (H) $^{13}C_1$ (α) tyrosinate. See Experimental Section for spectral conditions. Tick marks on the *y*-axis represent 0.04 absorbance units.

overlap with the natural abundance mode of interest ($c^{\%}_{j,k}$ in eq 2). As can be seen in Tables 3−6, $c^{\%}_{j,k}$ is usually >90%, but for certain modes and certain isotopologues (e.g., υ_{9a} in the deuterated isotopologues (Table 4)), the largest overlap can be much smaller, even less than 50%. In these cases, there is not a one-to-one correspondence between a given mode in the natural abundance spectrum ($\underline{B}_k$) and a mode in the isotopologue spectrum ($\underline{Q}_j$), rather the isotopologue mode in question is a linear combination of natural abundance modes. (Indeed this is always the case. It just so happens that often this linear combination is dominated by one vector, i.e., a certain $c_{j,k} \approx 1$ and the rest are ∼0.) This happens because changing the masses of the atoms in the system changes the mass-weighted coordinates used to calculate the normal modes and frequencies. As might be expected, this effect is most pronounced in the cases involving isotopologues with ^{2}H substitutions, since they change the mass weightings proportionally more than a ^{13}C substitution, for example. Thus, in Table 4, there are several modes that exhibit this "splitting" phenomena. Often, the mode with the largest overlap in these cases gives the best isotope shift compared to experiment (e.g., υ_{9a} in the 3′,5′-$^{2}H_2$ (ring) isotopologue), but modes with lower overlap can be important too (e.g., $\upsilon_{7a'}$ in the $^{2}H_4$ (ring) isotopologue).

While certain frequencies do show conformational sensitivity as noted above, isotope shifts on the other hand were found to be largely insensitive to conformation, and thus, only A conformation data is shown in the tables. The few significant exceptions to this are noted in the discussion below.

1656 cm^{-1}. Our calculations show that the broad peak at approximately 1656 cm^{-1} is an NH_2 bending mode of the tyrosinate amino group with some carboxylate asymmetric stretching character (see Figure 6a). The atomic displacement vectors in Figure 6a indicate that this mode involves a small degree of nitrogen motion, and thus, an $^{15}N_1$ isotope shift should be expected. The calculated spectrum shows just such a shift (Table 6). The broad nature of the peak in the experimental spectrum and interference from the water contributions makes this shift potentially visible only in the isotope-edited spectrum (Figure 5G).

This mode has been previously assigned as arising from residual water[58] and an NH_2 bending mode of the tyrosinate amino group.[22,54] The present calculations confirm this assignment, while also showing some carboxylate asymmetric stretching character (see Figure 6a).

1602 cm^{-1}. The calculations and spectra presented here show that the 1602 cm^{-1} band is the υ_{8a} ring stretching mode (Figure

TABLE 2: Tyrosinate Frequencies[a]

this work[b]	Nujol[c]	powder[d]	A	A′	B	B′	C	C′	assignment[e]
1656	*f*	1628	1688	1688	1665	1667	1671	1675	NH_2 bend/COO^- asym str
1602	1605	1608	1654	1654	1655	1655	1657	1655	υ_{8a}/NH_2 bend
1560	*f*	*g*	1643	1643	1677	1676	1665	1666	NH_2 bend/COO^- asym str
1500	1513	1514	1541	1541	1541	1543	1548	1546	υ_{19a}
1266	1212	*f*	1258	1259	1260	1260	1260	1258	$\upsilon_{7a'}$
1173	1176	*f*	1191	1191	1198	1196	1207	1202	υ_{9a}

[a] All frequencies are in cm^{-1}. Conformers are labeled by their symbol from Table 1. [b] See Methods for details. Experimental frequencies from Figure 3, with isotope sensitivity confirmed in Figure 5. [c] ref 53. [d] ref 54. [e] Approximate mode description and Wilson number where appropriate. Figure 6 illustrates the atom displacements for each mode. [f] Not available. [g] There are several peaks in the 1533−1590 cm^{-1} region, which Gabashvili et al.[54] assign as υ_{8b}, COO^-, and NH_2 or NH_3^+.

TABLE 3: Isotope Shifts of Tyrosinate Ring Carbon Isotopologues[a]

$^{13}C_1(4')$					$^{13}C_6$ (ring)					
exptl		calcd			exptl		calcd			
$\tilde{\nu}$	Δ	$\tilde{\nu}$	Δ	$c_{j,k}^{\%}$	$\tilde{\nu}$	Δ	$\tilde{\nu}$	Δ	$c_{j,k}^{\%}$	assignment
1656	0	1688	0	100	1656	0	1688	0	100	NH_2 bend/COO^- asym str
1599	−3	1648	−6	96	1549	−53	1596	−59	97	υ_{8a}/NH_2 bend
1556	−4	1643	0	98	1562	+2	1643	0	95	NH_2 bend/COO^- asym str
1491	−9	1533	−9	99	1464	−36	1503	−38	97	υ_{19a}
1242	−24	1234	−24	98	1238	−28	1227	−31	95	$\upsilon_{7a'}$
1172	−1	1191	0	99	1167	−6	1185	−7	92	υ_{9a}

[a] See Methods for details. Experimental frequencies from Figure 3, with isotope sensitivity confirmed in Figure 5.

TABLE 4: Isotope Shifts of Tyrosinate Deuterated Isotopologues[a]

$^2H_4$ (ring)					3′,5′-$^2H_2$ (ring)					
exptl		calcd			exptl		calcd			
$\tilde{\nu}$	Δ	$\tilde{\nu}$	Δ	$c_{j,k}^{\%}$	$\tilde{\nu}$	Δ	$\tilde{\nu}$	Δ	$c_{j,k}^{\%}$	assignment
1656	0	1688	0	100	1656	0	1688	0	100	NH_2 bend/COO^- asym str
1571	−31	1628	−26	90	1592	−10	1645	−10	59	υ_{8a}/NH_2 bend
					1592	−10	1641	−13	38	υ_{8a}/NH_2 bend
1557	−3	1643	0	93	1556	−4	1641	−2	60	NH_2 bend/COO^- asym str
					1556	−4	1645	+2	38	NH_2 bend/COO^- asym str
1420	−80	1458	−83	85	1455	−45	1501	−40	91	υ_{19a}
1236	−30	1238	−20	45	1259	−7	1250	−9	87	$\upsilon_{7a'}$
1236	−30	1135	−123	20						$\upsilon_{7a'}$
1236	−30	1221	−37	17						$\upsilon_{7a'}$
N/A[b]	N/A	888	−306	56	1063	−110	1077	−114	42	υ_{9a}
N/A	N/A	813	−378	16	1063	−110	863	−328	18	υ_{9a}
N/A	N/A	862	−329	14						υ_{9a}

[a] See Methods for details. Experimental frequencies from Figure 3, with isotope sensitivity confirmed in Figure 5. [b] Out of range.

TABLE 5: Isotope Shifts of Tyrosinate Oxygen Isotopologues[a]

$^{18}O_1$ (phenol)					$^{17}O_1$ (phenol)					
exptl		calcd			exptl		calcd			
$\tilde{\nu}$	Δ	$\tilde{\nu}$	Δ	$c_{j,k}^{\%}$	$\tilde{\nu}$	Δ	$\tilde{\nu}$	Δ	$c_{j,k}^{\%}$	assignment
1656	0	1688	0	100	1656	0	1688	0	100	NH_2 bend/COO^- asym str
1602	0	1654	0	100	1602	0	1654	0	100	υ_{8a}/NH_2 bend
1557	−3	1643	0	100	1562	+2	1643	0	100	NH_2 bend/COO^- asym str
1499	−1	1541	−1	100	1500	0	1541	0	100	υ_{19a}
1252	−14	1249	−9	99	1260	−6	1253	−5	100	$\upsilon_{7a'}$
1172	−1	1191	0	100	1172	−1	1191	0	100	υ_{9a}

[a] See Methods for details. Experimental frequencies from Figure 3, with isotope sensitivity confirmed in Figure 5.

6b), showing sensitivity to ^{13}C and ^2H labeling of the ring (Tables 3 and 4). There is good agreement between the calculated and observed isotope shifts. The calculations also reveal some NH_2 bending contributions (see Figure 6b); however, the calculated atomic displacements show very little nitrogen movement, in accordance with the calculated and experimental $^{15}N_1$ isotope shift (Table 6). However, in the B conformer, the $^{15}N_1$ isotope shift is calculated to be −1 cm^{-1}. These results are supported by previous work.[22,53,54]

1560 cm^{-1}. The band at 1560 cm^{-1} had been tentatively assigned as the υ_{8b} ring stretching mode,[22,54,55] with possible carboxylate asymmetric stretching contributions.[22,55] This assignment was supported by the reported isotope shifts of −4 cm^{-1} and −11 cm^{-1} in $^{13}C_1(4')$ and $^{13}C_6$ (ring), respectively.[22,55] As shown in Table 3, the current interpretation of the experimental spectrum gives isotope shifts of −4 cm^{-1} and +2 cm^{-1}, respectively, for these two isotopologues. Both of these interpretations are somewhat at odds with the present calculations that indicate very little ring atom motion for this mode (see Figure 6c) and predict isotope shifts of 0 cm^{-1}.

Previously unreported experimental isotope shifts for the $^2H_4$ and 3′,5′-$^2H_2$ isotopologues are −3 and −4 cm^{-1}, respectively,

TABLE 6: Isotope Shifts of Tyrosinate Backbone Isotopologues[a]

$^{15}N_1$					$^{13}C_1(\alpha)$					
exptl		calcd			exptl		calcd			
$\tilde{\nu}$	Δ	$\tilde{\nu}$	Δ	$c_{j,k}^{\%}$	$\tilde{\nu}$	Δ	$\tilde{\nu}$	Δ	$c_{j,k}^{\%}$	assignment
1656	0	1687	−1	100	1656	0	1688	0	100	NH_2 bend/COO^- asym str
1602	0	1654	0	100	1602	0	1654	0	100	υ_{8a}/NH_2 bend
1557	−3	1640	−3	98	1562	+2	1643	0	100	NH_2 bend/COO^- asym str
1500	0	1541	0	100	1500	0	1541	0	100	υ_{19a}
1265	−1	1258	0	100	1265	−1	1258	0	100	$\upsilon_{7a'}$
1173	0	1191	0	100	1173	0	1191	0	100	υ_{9a}

[a] See Methods for details. Experimental frequencies from Figure 3, with isotope sensitivity confirmed in Figure 5.

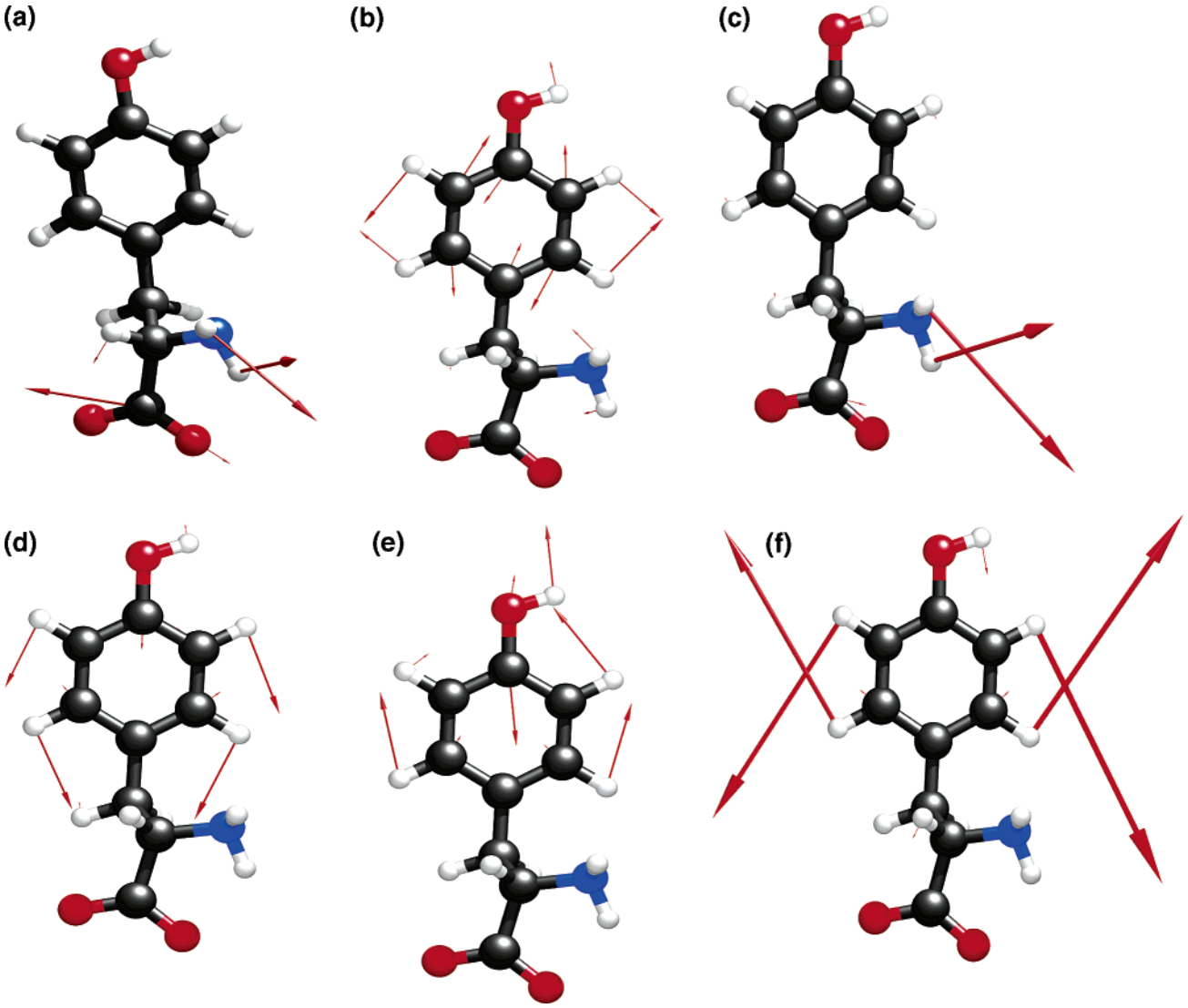

Figure 6. . Calculated tyrosinate atom displacements. Each mode is labeled as follows with its experimentally determined frequency in the natural abundance isotopologue: (a) 1656 cm^{-1} (NH_2 bend/COO^- asym str); (b) 1602 cm^{-1} (υ_{8a}/NH_2 bend); (c) 1560 cm^{-1} (NH_2 bend/COO^- asym str); (d) 1500 cm^{-1} (υ_{19a}); (3) 1266 cm^{-1} ($\upsilon_{7a'}$); (f) 1173 cm^{-1} (υ_{9a}). The displacement vectors are scaled to best reveal the essential motion of the mode in each case. As such, the magnitude of a displacement vector only has meaning relative to other vectors in that mode.

also indicating some ring hydrogen stretching character for this mode (see Figure 6c). The calculated shift is 0 cm^{-1} for the $^2H_4$ isotopologue and −2 cm^{-1} for the 3′,5′-$^2H_2$ isotopologue.

The experimental isotope shifts for the ^{18}O and ^{17}O isotopologues are inconsistent: −3 and +2 cm^{-1}, respectively (Table 5). Once again, since the calculated mode shows very little ring motion, the calculated isotope shifts for the heavy oxygen isotopologues are 0 cm^{-1}.

The ^{15}N isotopologue has an experimental isotope shift of −3 cm^{-1}, and the calculated shift is −3 cm^{-1} (Table 6). The $^{13}C_1(\alpha)$ isotopologue has a +2 cm^{-1} isotope shift in the experimental spectrum and 0 cm^{-1} in the calculated spectrum.

The calculated mode is dominated by NH_2 bending and carboxylate asymmetric stretching, with very little ring motion (see Figure 6c). Both of these contributions are in agreement with the experimental spectrum and the $^{15}N_1$ isotopologue shift. In the experimental spectra, the isotopologues with ring substitutions present a mixed picture, which seem to indicate some detectable ring motion. Therefore, we assign this band to

an NH_2 bend and carboxylate asymmetric stretch with possible ring stretching contributions.

As for υ_{8b}, there is no mode matching this description discernible in the experimental spectra if the 1560 cm^{-1} mode is assigned as an NH_2 bend. A possible υ_{8b} is calculated to occur at 1636 cm^{-1} with very little intensity.

1500 cm^{-1}. The band at 1500 cm^{-1} has been previously assigned as the υ_{19a} ring (Figure 6d) stretching mode.[22,53,54] The new experimental data and calculations confirm this assignment and are in remarkable agreement with each other for this mode. The observed ^{13}C ring, ^{2}H ring, $^{18}O_1$ phenol, and $^{17}O_1$ phenol isotope shifts are predicted accurately by our calculations (Tables 3−5).

1266 cm^{-1}. The band at 1266 cm^{-1} is due to the $\upsilon_{7a'}$ ring stretching mode (Figure 6e). This mode is essentially $C_4'-O$ stretching along with C−H deformation. As such a large isotope shift should be expected from $^{18}O_1$ or $^{17}O_1$ labeling of the phenol oxygen and ^{13}C labeling at the 4′ position, ^{13}C labeling on the remaining phenol carbons should produce only a small shift beyond labeling C_4'. All of these phenomena are present in both the experimental and calculated isotope shift data (Tables 3−5). The assignment of this band as $\upsilon_{7a'}$ is also supported by previous work.[12,13,22,23]

The B conformation has isotope shifts of −21, −26, −32, −8, and −8 cm^{-1} for $^{13}C_1$ (4′), $^{13}C_6$ (ring), $^{2}H_4$ (ring), 3′,5′-$^{2}H_2$ (ring), and $^{18}O_1$ (phenol) isotopologues respectively, which are qualitatively similar to the A conformer isotope shifts. In several cases, the B conformer isotope shifts are in better quantitative agreement with experiment ($^{13}C_6$ (ring), $^{2}H_4$ (ring), and 3′,5′-$^{2}H_2$ (ring)), illustrating the importance of conformational sampling in these calculations.

The $\upsilon_{7a'}$ mode is unique in that it is the only mode in the ground-state spectrum for which the calculated frequency (1258−1260 cm^{-1}) is *lower* than the experimentally observed frequency (1266 cm^{-1}) (compare with other modes in Table 2). Not only does this make $\upsilon_{7a'}$ different than the other modes in this work, it also runs counter to the observation that B3LYP systematically overpredicts frequencies.[36,59] Interestingly, $\upsilon_{7a'}$ appears at 1212 cm^{-1} when the spectrum is collected from a Nujol mull.[53] Additionally, when the phenol oxygen is deprotonated in the gas-phase calculations, this mode disappears completely due to the appearance of significant double-bond character in the phenol C−O bond (thus the need for the phenol hydrogen in the present calculations as discussed above). These two facts, when examined in light of the experimental conditions of this work (cryogenic polycrystalline matrix of high ionic strength versus the nonpolar environment in a Nujol mull), suggest that this mode is heavily influenced by the surrounding environment. This conclusion supports previous Raman studies of the effects of hydrogen bonding on the C−O vibration of tyrosine.[13]

1173 cm^{-1}. The small but distinctive band at 1173 cm^{-1} is due to the υ_{9a} ring stretching mode (Figure 6f). Dominated by ring C−H deformations, this mode exhibits large isotope shifts upon ^{2}H ring labeling as indicated in Table 4 and Figures 3 and 5. These results are supported by previous work.[22,53] Isotope shifts are also evident for ^{13}C ring labeling in the experimental spectra: −1 cm^{-1} for $^{13}C_1$ (4′) and −6 cm^{-1} for $^{13}C_6$ (ring). The calculated isotope shifts match experiment quite well: 0 cm^{-1} (A conformer) and −1 cm^{-1} (B conformer) for $^{13}C_1$ (4′) and −7 cm^{-1} (A conformer) and −8 cm^{-1} (B conformer) for $^{13}C_6$ (ring).

The experimental spectrum also shows small $^{18}O_1$ phenol and $^{17}O_1$ phenol isotope shifts, which are absent in the calculations.

TABLE 7: Tyrosyl Frequencies[a]

this work[b]	UVRR[c]	$\mathscr{A}$	$\mathscr{B}$	$\mathscr{C}$	$\mathscr{D}$	assignment
∼1556	1565	1614	1610	1621	1611	υ_{8a}
∼1516	1510	1530	1521	1541	1524	υ_{7a}

[a] All frequencies are in cm^{-1}. Conformers are labeled by their symbols from Table 1. [b] See Methods for details. Data from Figures 4 and 5. [c] Ultraviolet resonance Raman data from Johnson et al.[12]

Note that 1 cm^{-1} shifts are near the experimental detection limit given the spectral resolution and number of data points.

3.2.2. IR Spectra of Tyrosyl Radical Isotopologues. In examining the isotope-shifted spectra for positive intensity bands, which may arise from the radical, two bands are identified at ∼1556 and ∼1517 cm^{-1} in Figure 5 (see more detailed discussion below). Both of these modes show considerable (∼10−20 cm^{-1}) conformational dependence (Table 7), which may be a useful diagnostic for monitoring tyrosyl radical conformations on polypeptides. For example, when comparing conformer $\mathscr{A}$, the lowest-energy conformer, and $\mathscr{B}$, which may also be populated in the experiment (see discussion of conformation annealing above), a 4 cm^{-1} downshift of the 1556 cm^{-1} band and a 9 cm^{-1} downshift of the 1517 cm^{-1} band is predicted by the present calculations. Notice that the $^{18}O_1$ and $^{17}O_1$ isotopologues show small but well-resolved positive bands at ∼1603, ∼1498, and ∼1425 cm^{-1}, which are isotope-sensitive. The assignment of these bands is not considered here.

The calculations predict that υ_{8b} (Figure 7d) has negligible intensity in the radical and that υ_{19a} appears at ∼1431 cm^{-1} (Figure 7c). Also of note is a predicted shift in NH_2 bend/COO^- asymmetric stretching modes upon oxidation. These modes shift from 1688 and 1642 cm^{-1} in the singlet $\mathscr{A}$ conformer to 1697 and 1647 cm^{-1} in the tyrosyl radical $\mathscr{A}$ conformer and from 1665 and 1677 cm^{-1} in the singlet B conformer to 1667 and 1669 cm^{-1} in the radical $\mathscr{B}$ conformer. Both of these modes have calculated $^{15}N_1$ isotope shifts of −4 and 0 cm^{-1}, respectively, in the radical, in agreement with the experimentally observed $^{15}N_1$ isotope sensitivity.[22]

As in the singlet state, isotope shifts of the radical are largely insensitive to conformation, and thus, only $\mathscr{A}$ conformation data is shown in the tables. The few significant exceptions to this are noted in the discussion below.

∼1556 cm^{-1}. In previous Raman experiments on tyrosyl radical, this band has been assigned at ∼1565 cm^{-1}.[12] Our calculations (Tables 7 and 8) place this mode at 1610−1621 cm^{-1} in the natural abundance spectrum and predict isotope shifts of −54 cm^{-1} for the $^{13}C_6$ isotopologue. These results are in good agreement with the calculations of Qin and Wheeler,[16] in which this mode was placed at 1620 cm^{-1}, with a predicted isotope shift of −56 cm^{-1}. As shown in (Tables 7 and 8), isotope shifts in the deuterated isotopologues are calculated to be −38 cm^{-1} and −10 cm^{-1} for the $^{2}H_4$ and 3′,5′-$^{2}H_2$ isotopologues, respectively. No isotope shifts are predicted by the calculations for the $^{13}C_1$ (4′), $^{18}O_1$ (phenol), $^{17}O_1$ (phenol), $^{13}C_1(\alpha)$, or $^{15}N_1$ isotopologues.

In our difference spectra, which are associated with tyrosinate photolysis, there is a broad negative intensity band at ∼1550 cm^{-1}, which originates from a perturbation of NH_2 bending/COO asymmetric stretching vibration with tyrosine oxidation (Figure 4). Apparently, this band obscures the positive υ_{8a} tyrosyl radical mode, which is not obvious in the difference spectra. Therefore, potential isotope shifts in this band have to be evaluated from the isotope-edited spectra (Figure 5). Many of the isotope-shifted spectra exhibit a positive band between 1549 and 1560 cm^{-1}, which is a candidate for this expected tyrosyl

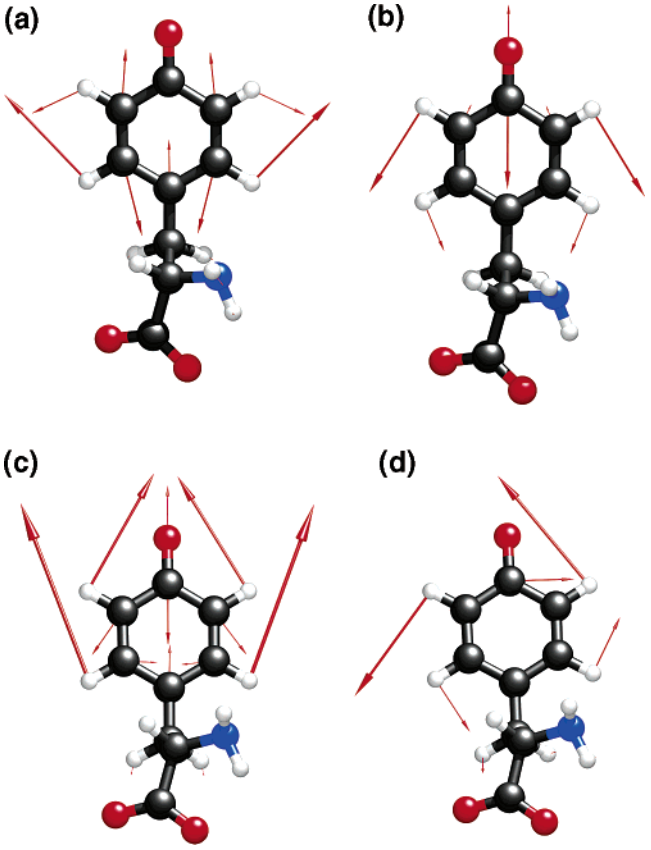

Figure 7. Calculated tyrosyl radical atom displacements. Each mode is labeled as follows with its experimentally determined frequency in the natural abundance isotopologue except where noted: (a) ~1556 cm^{-1} (υ_{8a}); (b) ~1517 cm^{-1} (υ_{7a}); (c) 1431 cm^{-1} (υ_{19a}) (calculated); (d) 1278 cm^{-1} (υ_{8b}) (calculated). The displacement vectors are scaled to best reveal the essential motion of the mode in each case. As such, the magnitude of a displacement vector only has meaning relative to other vectors in that mode.

TABLE 8: Calculated Isotope Shifts Tyrosyl Isotopologues

$^{13}C_1$ (4′)			$^{13}C_6$ (ring)			
$\tilde{\nu}$	Δ	$c^{\%}_{j,k}$	$\tilde{\nu}$	Δ	$c^{\%}_{j,k}$	assignment
1614	0	100	1559	−54	99	υ_{8a}
1502	−27	95	1490	−40	94	υ_{7a}
$^{2}H_4$ (ring)			3′,5′-$^{2}H_2$ (ring)			
$\tilde{\nu}$	Δ	$c^{\%}_{j,k}$	$\tilde{\nu}$	Δ	$c^{\%}_{j,k}$	assignment
1576	−38	95	1603	−10	98	υ_{8a}
1507	−23	86	1508	−22	89	υ_{7a}
$^{18}O_1$ (phenol)			$^{17}O_1$ (phenol)			
$\tilde{\nu}$	Δ	$c^{\%}_{j,k}$	$\tilde{\nu}$	Δ	$c^{\%}_{j,k}$	assignment
1613	0	100	1614	0	100	υ_{8a}
1516	−14	98	1522	−8	99	υ_{7a}
$^{15}N_1$			$^{13}C_1(\alpha)$			
$\tilde{\nu}$	Δ	$c^{\%}_{j,k}$	$\tilde{\nu}$	Δ	$c^{\%}_{j,k}$	assignment
1614	0	100	1614	0	100	υ_{8a}
1530	0	100	1530	0	100	υ_{7a}

radical υ_{8a}. Except in the case of the $^{2}H_4$ and 3′,5′-$^{2}H_2$ ring isotopologues (Figure 4E,F), the location of the isotope-shifted υ_{8a} band is not obvious in the difference or in the isotope-edited spectra, perhaps because the downshifted band broadens.

However, in the $^{2}H_4$ and 3′,5′-$^{2}H_2$ ring isotopologues (Figure 4E,F), the difference spectra exhibit a new shoulder at 1527 cm^{-1}, which is not observed in the natural abundance spectrum (Figure 4B). This 1527 cm^{-1} band most likely corresponds to the expected isotope-shifted υ_{8a} band and is also apparent in the isotope-edited data (Figure 5C,D). The magnitude of the observed isotope-induced downshift (−25 cm^{-1}, as estimated from the isotope-edited spectrum) for this $^{2}H_4$ isotopologue is smaller than the value predicted in Table 8 (−38 cm^{-1}). For the 3′,5′-$^{2}H_2$ isotopologue, the experimental value is greater than the theoretical prediction (−29 cm^{-1} exptl versus −10 cm^{-1} calcd).

On the basis of the results with the $^{2}H_4$ and 3′,5′-$^{2}H_2$ ring isotopologues, the ~1556 cm^{-1} band is assigned to the υ_{8a} ring stretching mode of the radical (Figure 7a and Table 8). However, this question must be revisited with the other isotopologues through resonance Raman spectroscopy. It is not possible to calculate a pure spectrum of the radical from the difference FT-IR spectrum, because the negative intensity bands do not correspond in frequency and amplitude to the singlet spectrum. Only bands perturbed by photolysis will be observed in the difference FT-IR spectrum, and this is most likely a subset of the observed features in the singlet absorption spectrum.

~1516 cm^{-1}. In the ultraviolet resonance Raman spectra of Johnson et al.,[12] a band at 1510 cm^{-1} was assigned as the υ_{7a} C−O stretching band. A positive 1516 cm^{-1} band is observed in the difference FT-IR spectrum, associated with tyrosinate photolysis (Figure 4B). Assignment of this band can be based on a comparison of experimentally observed (Figures 4 and 5) and calculated isotope shifts.

The isotope shifts of the 1516 cm^{-1} band can be determined from the difference spectra for many of the isotopologues. For example, the band at 1516 cm^{-1} is observed to shift to 1480 cm^{-1} in the $^{13}C_6$ (ring) isotopologue (Figure 4D) to 1493 cm^{-1} in the $^{2}H_4$ (ring) isotopologue (Figure 4E) and to be insensitive to isotope substitution in the $^{15}N_1$ isotopologue (Figure 4I). In the case of the $^{13}C_1$ (4′), 3′,5′-$^{2}H_2$ (ring), $^{18}O_1$ (phenol), and $^{17}O_1$ (phenol) isotopologues, the difference spectra (Figure 4C, F, G, H) show a decrease in amplitude for the 1516 cm^{-1} band, but the location of the isotope-shifted line is not obvious. For the $^{18}O_1$ (phenol), and $^{17}O_1$ (phenol) isotopologues, the magnitude of the isotope shift can be determined from the double difference spectra (Figure 5E and F) and is observed to be −12 cm^{-1} in the $^{18}O_1$ (phenol) isotopologue and −10 cm^{-1} in the $^{17}O_1$ (phenol) isotopologue.

The locations of the downshifted 1516 cm^{-1} band are not clear in spectra acquired from the $^{13}C_1$ (4′) isotopologue, even in the isotope-edited spectrum (Figure 5A) and from the 3′,5′-$^{2}H_2$ (ring) isotopologue, in which two candidate downshifted bands are observed in the difference spectrum (Figure 4F). In the case of the 3′,5′-$^{2}H_2$ (ring) isotopologue, one of the new bands, at 1497 cm^{-1}, gives an isotope shift similar to the calculated one (19 cm^{-1} versus 22 cm^{-1} predicted in Table 8). In the case of the $^{13}C_1(\alpha)$ isotopologue, isotope shifts of −2 to −6 cm^{-1} are observed in the difference and double difference spectra, respectively (Figures 4J and 5H).

To compare the experimentally observed isotope shifts (in cm^{-1}) with the results of our calculations (Table 8): $^{13}C_6$ (ring), −36 exptl/−40 calcd; $^{2}H_4$ (ring), −23 exptl/−23 calcd; $^{18}O_1$ (phenol), −12 exptl/−14 calcd; $^{17}O_1$ (phenol), −10 exptl/−8 calcd; $^{15}N_1$, 0 exptl/0 calcd; $^{13}C_1(\alpha)$, −6 to −2 exptl/0 calcd. Overall, this is excellent agreement between experiment and calculations, with the calculations possibly underestimating the amount of mechanical coupling between the C−O stretching

and carbon backbone vibrational modes. This comparison allows a definitive assignment of the 1516 cm^{-1} band to υ_{7a} (Figure 7b) in the radical.

The ~300 cm^{-1} upshift of this vibrational band, when compared to the singlet state, indicates that there is a significant change in C−O bond character between the singlet and the radical. Indeed, natural bond orbital analysis[44] at the B3LYP/6-311++G(3df,2p)//B3LYP/6-31++G(d,p) level gives bond orders of 0.98 and 1.50 for the singlet and radical species, respectively. This large upshift is in agreement with previous observations.[11−14]

3.3. Applicability to Enzymatic Systems. These calculations, showing the assignments and conformational dependence of tyrosine and tyrosyl radical vibrational frequencies, are expected to apply to redox-active tyrosines in enzymes. In this application, there are two different issues to consider, one concerning the ring dihedral angle and the other the backbone dihedral angle. It might be imagined that the barrier to ring rotation is relatively shallow in proteins. However, the EPR spectrum of tyrosyl radical is sensitive to changes in this dihedral angle.[9] Previous EPR studies of PSII tyrosyl radicals show that, even at high temperatures, the EPR line shape is broadened because of restrictions in ring rotational mobility.[3] In addition, different conformational preferences for the ring dihedral angle are shown in different enzymes. For example, when the $Y_Z^{\bullet}$ PSII tyrosyl radicals are compared to the $Y_{122}^{\bullet}$ radical in *E. coli* ribonucleotide reductase, the EPR line shape reflects a difference in dihedral angle, which is imposed on the aromatic side chain by protein packing forces.[9] On the other hand, the dihedral angles observed in PSII tyrosyl radicals are similar to the dihedral angles observed in model compounds.[9] Note that changes in conformation have been observed upon tyrosyl radical formation in ribonucleotide reductase.[60]

The influence of peptide bond formation and protein packing on the backbone dihedral angle can also be considered, to evaluate the applicability of our potential energy calculations. Tyrosine main chain dihedral angles have been catalogued in existing protein structures.[61] According to this analysis, the backbone dihedral angle is divided into three regions, $\bar{g}$, which is equivalent to our A, A′, and $\mathscr{A}$ conformers, g^+, which is equivalent to our B, B′, and $\mathscr{B}$ conformers, and *t*, which is equivalent to our C, C′, $\mathscr{C}$, and $\mathscr{D}$ conformers (as in Table 1, calligraphic letters refer to the radical potential energy surface). After surveying known protein structures, ref 61 concludes that tyrosine side chains in proteins are found in the following conformations: 13% in the A,A′ conformers, 55% in the B,B′ conformers, and 32% in the C,C′ conformations. Our calculations for model tyrosinate predict that the A and B conformers are lowest and similar in energy (Table 1). Therefore, this comparison suggests that our tyrosinate calculations are reasonably predictive for proteins, because our lowest-energy conformers correspond to ~70% of the observed tyrosine conformers found in X-ray crystal structures.[61] Field-swept EPR spectroscopy is not a good reporter of backbone dihedral angle.[22] Therefore, the conformational dependence of FT-IR frequencies provides a potentially important probe of the structure of redox-active tyrosines in enzymes.

3.4. Conformation of an Enzymatic Tyrosyl Radical, $Y_Z^{\bullet}$, in PSII. Reaction-induced FT-IR spectra of $Y_Z^{\bullet}$ can be analyzed in light of these considerations. In an earlier publication, reaction-induced FT-IR spectra, associated with the oxidation of Y_Z in PSII, were presented.[24] To measure these spectra, PSII was stripped of its active site manganese. This treatment slows $Y_Z^{\bullet}$ reduction and allows the radical to be photoaccumulated.[62] The published data were obtained at 263 K, and the PSII redox-active tyrosine was $^2H_4$ (ring)-labeled to generate isotope-edited spectra.[24] These $Y_Z^{\bullet}$ spectra can be compared to model $^2H_4$ (ring) tyrosine FT-IR spectra (acquired at 77 K) and to our calculations.

To reiterate, our calculations predict that the frequencies of υ_{8a} and υ_{7a} tyrosyl radical bands are conformation sensitive (Table 7). In the isotope-edited spectrum from the model tyrosyl radical (Figure 5C), υ_{8a} is observed at 1552 cm^{-1}, and an isotope shift to 1527 cm^{-1} (Δ = 25 cm^{-1}) is observed in $^2H_4$ (ring) labeled tyrosyl radical. Because this model tyrosinate experiment was performed at 77 K, the represented conformers are expected to be in the A/A′ and B/B′ conformations, corresponding to the lowest-energy conformers in Table 1, which will be frozen under cryogenic conditions.

On the other hand, in the isotope-edited spectrum from $Y_Z^{\bullet}$, υ_{8a} is observed at 1558 cm^{-1} and exhibits an isotope shift to 1547 cm^{-1} (Δ = 11 cm^{-1}).[24] The altered frequency is consistent with a difference in conformational preference in the $Y_Z^{\bullet}$ compared to model tyrosyl radical at 77 K.

To interpret the higher ring stretching frequency of $Y_Z^{\bullet}$, we compare to the frequency to trends in our calculated frequencies for tyrosyl radical (Table 7). These calculations show that the $\mathscr{B}$ and $\mathscr{D}$ conformers in model tyrosyl radical have similar frequencies and that these frequencies are the lowest of the radical conformational states. For example, the $\mathscr{A}$ conformer frequency is 4 cm^{-1} higher, and the $\mathscr{C}$ conformer frequency is 11 cm^{-1} higher, when compared to the $\mathscr{B}$ conformer (Table 7). Because the $\mathscr{A}$ and $\mathscr{B}$ conformations are present in model tyrosyl radical, with its 1552 cm^{-1} υ_{8a} frequency, these calculations suggest that $Y_Z^{\bullet}$, with a υ_{8a} frequency of 1558 cm^{-1}, must be in the $\mathscr{C}$ conformation. This conclusion is in agreement with a 3.0 Å PSII structure.[63]

The CO stretching vibration of $Y_Z^{\bullet}$ is much lower in frequency (1478 cm^{-1}), when compared to model tyrosyl radical (1516 cm^{-1}) (reviewed in ref 4). While the $\mathscr{C}$ conformer would be expected to have the highest C−O frequency (Table 7), the perturbed, downshifted C−O frequency of $Y_Z^{\bullet}$ has been previously attributed to an intermolecular interaction with the phenol oxygen in the protein environment.

4. Conclusion

In this paper, the normal modes of several conformations of tyrosinate and tyrosyl radical are presented at the B3LYP/6-31++G(d,p) level of theory. This level of theory successfully predicts the vibrational spectrum of phenoxyl radical in an argon matrix. For tyrosinate, three stable conformers are predicted; two will be populated significantly at room temperature. For tyrosyl radical, four stable conformers are predicted, one of which is >2.5 kcal/mol below the other three in energy. These predictions support previous EPR and ESEEM studies of tyrosyl radical conformation at cryogenic temperature[51] and explain the spontaneous conformational changes observed upon annealing in the radical.[52]

Results suggest that the frequencies of all singlet and radical normal modes show some dependence on conformation. The largest shifts (>20 cm^{-1}) are observed for the tyrosinate NH_2 bend/COO^- asymmetric stretching mode at 1560 cm^{-1} and the C−O stretching vibration of the radical at 1510 cm^{-1}. Substantial shifts (>10 cm^{-1}) are also observed for the tyrosinate NH_2 bending/COO^- asymmetric stretching mode at 1650 cm^{-1}, the tyrosinate υ_{9a} bending vibration at 1173 cm^{-1}, and the 1556 cm^{-1} υ_{8a} ring vibration of the radical. These findings are

important because they suggest that selected vibrational bands of singlet and radical state may eventually be used to determine the conformation of redox active tyrosines in complex protein environments. Further, the vibrational spectrum may be used to probe for conformation reorientation upon tyrosine oxidation, which is known to occur in ribonucleotide reductase.[60]

When experiment and theory are compared, it is found that the predicted frequencies are in good agreement when the systematic over prediction of frequencies by B3LYP and other limitations of the computational model are considered. The agreement for the predicted isotope shifts is excellent for the singlet vibrational spectrum, with theory consistently slightly underestimating the coupling between terminal groups and the aromatic ring. This trend of underestimating the coupling is also observed for the radical. Comparison with experiment also suggests that the υ_{7a}' and υ_{9a} frequencies in the singlet and the υ_{7a} frequency in the radical are perturbed by a nonbonding interaction, which is probably due to hydrogen bonding with the solvent. There is also excellent agreement between the calculated and experimental frequencies and isotope shifts for the tyrosyl radical C−O stretching vibration.

Taken together, these results are consistent with previous calculations, which predicted a conformation-dependent spin delocalization to the tyrosine amino group. Here, the effect on the NH_2 bending mode is to perturb the frequency in a conformationally dependent way.

These calculations represent the most rigorous examination of the normal modes of tyrosinate and tyrosyl radical and their various conformations and isotopologues. In combination with the experimental spectra of a comprehensive array of isotopologues also presented here, these results establish an extensive spectroscopic fingerprint for these systems in the infrared from 1650 to 1100 cm^{-1}. These fingerprint data should facilitate interpretation of tyrosine-originating spectral features in more complex environments such as enzymes.

Acknowledgment. The authors are grateful for financial support provided by the National Institutes of Health grants GM 62248 (D.Y.) and GM 43273 (B.A.B.). D.Y. acknowledges the Army High Performance Computing Research Center (AHPCRC) under the auspices of the Department of the Army, Army Research Laboratory (ARL), under Cooperative Agreement number DAAD19-01-2-0014. Computational resources were provided by the Minnesota Supercomputing Institute.

Supporting Information Available: Table S1: Selected Bond Lengths and Bond Angles of Phenoxyl Radical. Table S2: Vibrations of Phenoxyl Radical. Appendix: B3LYP/6-31++G(d,p) coordinates. This material is available free of charge via the Internet at http://pubs.acs.org.

References and Notes

(1) Smith, W. L.; Eling, T. E.; Kulmacz, R. J.; Marnett, L. J.; Tsaii, A. *Biochemistry* **1992**, *31*, 3−7.
(2) Larsson, A.; Sjoberg, B. M. *EMBO J.* **1986**, *5*, 2037−2040.
(3) Barry, B. A.; Babcock, G. T. *Proc. Natl. Acad. Sci. U.S.A.* **1987**, *84*, 7099−7103.
(4) Pujols-Ayala, I.; Barry, B. A. *Biochim. Biophys. Acta* **2004**, *1655*, 205−216.
(5) Barry, B. A.; Einarsdóttir, O. *J. Phys. Chem. B* **2005**, *109*, 6972−6981.
(6) Box, H. C.; Budzinski, E. E.; Freund, H. G. *J. Chem. Phys.* **1974**, *61*(6), 2222−2226.
(7) Dixon, W. T.; Moghimi, M.; Murphy, D. *J. Chem. Soc., Faraday Trans. 2* **1974**, *70*, 1713−1720.
(8) Sealy, R. C.; Harman, L.; West, P. R.; Mason, R. P. *J. Am. Chem. Soc.* **1985**, *107*(12), 3401−3406.
(9) Barry, B. A.; El-Deeb, M. K.; Sandusky, P. O.; Babcock, G. T. *J. Biol. Chem.* **1990**, *265*, 20139−20143.
(10) Hulsebosch, R. J.; van den Brink, J. S.; Nieuwenhuis, S. A. M.; Gast, P.; Raap, J.; Lugtenburg, J.; Hoff, A. J. *J. Am. Chem. Soc.* **1997**, *119*, 8685−8694.
(11) Tripathi, G. N. R.; Schuler, R. H. *J. Chem. Phys.* **1984**, *81*, 113−121.
(12) Johnson, C. R.; Ludwig, M.; Asher, S. A. *J. Am. Chem. Soc.* **1986**, *108*, 905−912.
(13) Takeuchi, H.; Watanabe, N.; Satoh, Y.; Harada, I. *J. Raman Spectrosc.* **1989**, *20*(4), 233−237.
(14) Mukherjee, A.; McGlashen, M. L.; Spiro, T. G. *J. Phys. Chem.* **1995**, *99*, 4912−4917.
(15) Qin, Y.; Wheeler, R. A. *J. Chem. Phys.* **1995**, *102*, 1689−1698.
(16) Qin, Y.; Wheeler, R. A. *J. Am. Chem. Soc.* **1995**, *117*, 6083−6092.
(17) Qin, Y.; Wheeler, R. A. *J. Phys. Chem.* **1996**, *100*, 10554−10563.
(18) O'Malley, P.; Ellson, D. *Biochim. Biophys. Acta* **1997**, *1320*, 65−72.
(19) Himo, F.; Gräslund, A.; Eriksson, L. A. *Biophys. J.* **1997**, *72*, 1556−1567.
(20) Nwobi, O.; Higgins, J.; Zhou, X.; Liu, R. *Chem. Phys. Lett.* **1997**, *272*, 155−161.
(21) Wise, K. E.; Pate, J. B.; Wheeler, R. A. *J. Phys. Chem. B* **1999**, *103*, 4764−4772.
(22) Ayala, I.; Range, K.; York, D.; Barry, B. A. *J. Am. Chem. Soc.* **2002**, *124*, 5496−5505.
(23) O'Malley, P. J. *Biochim. Biophys. Acta* **2002**, *1553*, 212−217.
(24) Pujols-Ayala, I.; Sacksteder, C. A.; Barry, B. A. *J. Am. Chem. Soc.* **2003**, *125*, 7536−7538.
(25) Becke, A. D. *Phys. Rev. A.* **1988**, *38*, 3098−3100.
(26) Becke, A. D. *J. Chem. Phys.* **1993**, *98*(7), 5648−5652.
(27) Lee, C.; Yang, W.; Parr, R. G. *Phys. Rev. B* **1988**, *37*, 785−789.
(28) Frisch, M. J.; Pople, J. A.; Binkley, J. S. *J. Chem. Phys.* **1984**, *80*, 3265−3269.
(29) Frisch, M. J.; Trucks, G. W.; Schlegel, H. B.; Scuseria, G. E.; Robb, M. A.; Cheeseman, J. R.; Zakrzewski, V. G.; Montgomery, J. A., Jr.; Stratmann, R. E.; Burant, J. C.; Dapprich, S.; Millam, J. M.; Daniels, A. D.; Kudin, K. N.; Strain, M. C.; Farkas, O.; Tomasi, J.; Barone, V.; Cossi, M.; Cammi, R.; Mennucci, B.; Pomelli, C.; Adamo, C.; Clifford, S.; Ochterski, J.; Petersson, G. A.; Ayala, P. Y.; Cui, Q.; Morokuma, K.; Malick, D. K.; Rabuck, A. D.; Raghavachari, K.; Foresman, J. B.; Cioslowski, J.; Ortiz, J. V.; Stefanov, B. B.; Liu, G.; Liashenko, A.; Piskorz, P.; Komaromi, I.; Gomperts, R.; Martin, R. L.; Fox, D. J.; Keith, T.; Al-Laham, M. A.; Peng, C. Y.; Nanayakkara, A.; Gonzalez, C.; Challacombe, M.; Gill, P. M. W.; Johnson, B. G.; Chen, W.; Wong, M. W.; Andres, J. L.; Head-Gordon, M.; Replogle, E. S.; Pople, J. A. *Gaussian 98*, revision A.9; Gaussian, Inc.: Pittsburgh, PA, 1998.
(30) Frisch, Æ.; Frisch, M. J.. *Gaussian 98 User's Reference*, 2nd e.; Gaussian, Inc.: Pittsburgh, PA, 1999.
(31) Peng, C.; Ayala, P. Y.; Schlegel, H. B.; Frisch, M. J. *J. Comput. Chem.* **1996**, *17*, 49−56.
(32) Adamo, C.; Barone, V.; Fortunelli, A. *J. Chem. Phys.* **1995**, *102*, 384−393.
(33) Razeghifard, M. R.; Kim, S.; Patzlaff, J. S.; Hutchison, R. S.; Krick, T.; Ayala, I.; Steenhuis, J. J.; Boesch, S. E.; Wheeler, R. A.; Barry, B. A. *J. Phys. Chem. B* **1999**, *103*, 9790−9800.
(34) Montgomery, J. A., Jr.; Frisch, M. J.; Ochterski, J. W.; Petersson, G. A. *J. Chem. Phys.* **1999**, *110*(6), 2822−2827.
(35) Baboul, A. G.; Curtiss, L. A.; Redfern, P. C.; Raghavachari, K. *J. Chem. Phys.* **1999**, *110*, 7650−7657.
(36) Martin, J. M. L.; de Oliveira, G. *J. Chem. Phys.* **1999**, *111*, 1843−1856.
(37) López, C. S.; Faza, O. N.; de Lera, A. R.; York, D. M. *Chem.−Eur. J.* **2005**, *11*, 2081−2093.
(38) Mayaan, E.; Range, K.; York, D. M. *J. Biol. Inorg. Chem.* **2004**, *9*(7), 807−817.
(39) López, C. S.; Faza, O. N.; Gregersen, B. A.; Lopez, X.; de Lera, A. R.; York, D. M. *ChemPhysChem* **2004**, *5*, 1045−1049.
(40) Range, K.; McGrath, M. J.; Lopez, X.; York, D. M. *J. Am. Chem. Soc.* **2004**, *126*, 1654−1665.
(41) Chipman, D. M.; Liu, R.; Zhou, X.; Pulay, P. *J. Chem. Phys.* **1994**, *100*(7), 5023−5035.
(42) Spanget-Larsen, J.; Gil, M.; Gorski, A.; Blake, D. M.; Waluk, J.; Radziszewski, J. G. *J. Am. Chem. Soc.* **2001**, *123*, 11253−11261.
(43) Grafton, A. K.; Wheeler, R. A. *J. Comput. Chem.* **1998**, *19*(14), 1663−1674.
(44) Foster, J. P.; Weinhold, F. *J. Am. Chem. Soc.* **1980**, *102*, 7211−7218.
(45) Reed, A. E.; Weinstock, R. B.; Weinhold, F. *J. Chem. Phys.* **1985**, *83*, 735−746.
(46) Vassiliev, I. R.; Offenbacher, A. R.; Barry, B. A. *J. Phys. Chem. B* **2005**, *109*, 23077−23085.
(47) Berthomiev, C.; Boussac, A. *Biospectroscopy* **1995**, *1*, 187−206.

(48) Ahlbrink, R.; Haumann, M.; Cherepanov, D.; Bögershausen, O.; Mulkidjanian, A.; Junge, W. *Biochemistry* **1998**, *37*, 1131−1142.
(49) Wang, Y.-N.; Eriksson, L. A. *Int. J. Quantum Chem.* **2001**, *83*, 220−229.
(50) Cramer, C. J. *Essentials of Computational Chemistry: Theories and Models*, 2nd ed.; John Wiley & Sons: Chichester, England, 2004.
(51) Warncke, K.; Babcock, G. T.; McCracken, J. *J. Phys. Chem.* **1996**, *100*, 4654−4661.
(52) Warncke, K.; Perry, M. S. *Biochim. Biophys. Acta* **2001**, *1545*, 1−5.
(53) Grace, L. I.; Cohen, R.; Dunn, T. M.; Lubman, D. M.; de Vries, M. S. *J. Mol. Spectrosc.* **2002**, *215*(2), 204−219.
(54) Gabashvili, I.; Menikh, A.; Ségui, J.; Fragata, M. *J. Mol. Struct.* **1998**, *444*, 123−133.
(55) Cappuccio, J. A.; Ayala, I.; Elliott, G. I.; Szundi, I.; Lewis, J.; Konopelski, J. P.; Barry, B. A.; Einarsdóttir, O. *J. Am. Chem. Soc.* **2002**, *124*, 1750−1760.
(56) Tsuboi, M.; Kubo, Y.; Ikeda, T.; Overman, S. A.; Osman, O.; Thomas, G. J., Jr. *Biochemistry* **2003**, *42*, 940−950.
(57) Tsuboi, M.; Overman, S. A.; Nakamura, K.; Rodriguez-Casado, A.; Thomas, G. J., Jr. *Biophys. J.* **2003**, *34*, 1969−1976.
(58) Bellamy, L. J. *The infrared spectra of complex molecules*; Chapman and Hall: London, 1980.
(59) Cramer, C. J. *Essentials of Computational Chemistry: Theories and Models*, 2nd ed.; John Wiley & Sons: Chichester, England, 2002.
(60) Högbom, M.; Galander, M.; Andersson, M.; Kolberg, M.; Hofbauer, W.; Lassmann, G.; Nordlund, P.; Lendzian, F. *Proc. Natl. Acad. Sci. U.S.A.* **2003**, *100*, 3209−3214.
(61) Chakrabarti, P.; Pal, D. *Protein Eng.* **1998**, *11*, 631−647.
(62) Barry, B. A. *Methods Enzymol.* **1995**, *258*, 303−319.
(63) Loll, B.; Kern, J.; Saenger, W.; Zouni, A.; Biesiadka, J. *Nature (London)* **2005**, *438*, 1040−1044.